First-Principles Study on the Direct Bandgap Double Perovskite Series Cs_2LiInX_6(X = F, Cl, and Br)

Jiaolian Luo,* Anqi Yang, and Zhenyu Xie

Read Online

ACCESS | Metrics & More | Article Recommendations

ABSTRACT: A molecular crystal structure model of the lead-free halide chalcogenide semiconductor Cs_2LiInX_6 (X = F, Cl, and Br) was established, and its energy band, density of states, optical properties, and thermodynamic properties were calculated using the first nature principle and the effect of different pressures on the bandgap of Cs_2LiInX_6 (X = F and Cl, Cs_2LiInF_6 with a bandgap of 7.359 eV, $Cs_2LiInCl_6$ with a bandgap of 5.098 eV, and $Cs_2LiInBr_6$ with a bandgap of 3.755 eV). The absorption of light is mainly due to the transition of halide ions from p- to s-orbitals. The p- and In-s orbitals of halide ions play a major role in light harvesting. $Cs_2LiInCl_6$ has low sensitivity to relative pressure and is stable at a 0−100 GPa pressure. In the structure of Cs_2LiInX_6 (X = F, Cl, and Br), changing the halogen atom can effectively improve its optical properties. $Cs_2LiInCl_6$ and Cs_2LiInF_6 are considered as the most promising candidates for UV detectors. Cs_2LiInF_6 has a large forbidden

band width and a high Debye temperature and shows a high photoluminescence quantum yield in the field of phosphors with great potential in the field of phosphors with high photoluminescence quantum yields. This study is a positive reference for the preparation of lead-free chalcogenide-type ultraviolet detectors with excellent performance.
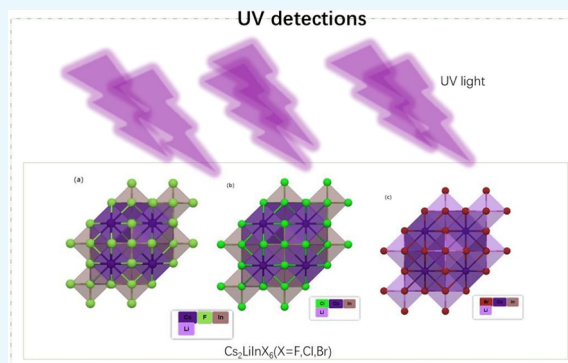
1. INTRODUCTION

Ultraviolet photodetectors have attracted extensive attention in many fields, and are very important for many industrial and military applications.[1−6] High sensitivity, high detection rate, fast response speed, high spectral selectivity, and high stability are the requirements for an ideal UV photodetector. Although various traditional semiconductor materials have been successfully used, such as Si, ZnO, TiO_2, SnO_2, Ga2O3, GaN, etc., their wide application is hindered by expensive initial manufacturing costs and mechanical inflexibility. Therefore, it is very important to find new materials for the next generation of high-performance UV detection. Halide perovskite materials have attracted extensive attention because of their unique physicochemical properties and good photoelectric properties.[7−10] At the same time, halide peroxides have been proven to be outstanding candidates for photoelectric devices. In general, typically mixed halide perovskites adopt an ABX_3 crystal structure, where A, B, and X employ organic cations (e.g., $CH_3NH_3^+$), metal cations (Pb^{2+}), and halide anions (I^-, Br^-, Cl^-, or a mixture of them), respectively.[11−13] With their long carrier two-dimensional fusion length, high defect tolerance, long carrier lifetime, and high absorption coefficients, perovskite materials have enabled a large number of optoelectronic devices.[14−16] Despite all these remarkable successes, much perovskite-based optoelectronics suffer from the inherent instability of the organic components and the

toxicity of Pb^{2+}, which are the two key components in the most commonly used halide-based organic−inorganic hybrid perovskites. This has largely limited their practical applications. Although metal halide perovskite has low-cost solution treatment, excellent defect tolerance, and visible spectrum of tunable emission, lead halide perovskite still faces significant challenges, such as from long time exposure to light, humidity, high-temperature instability caused by the environment, and the inherent toxicity of lead (and its biological accumulation in the ecosystem). These problems seriously hinder the application of organic−inorganic hybrid perovskite. This has prompted the material researchers to search for non-toxic, stable, and efficient metal halide perovskite materials with similar photoelectric properties.

In recent studies, it has been suggested that double perovskite A_2BReX_6 (where one B and one Re replace two toxic Pb^{2+}) is a stable and non-toxic alternative to lead halide perovskite without the addition of toxic elements such as lead,
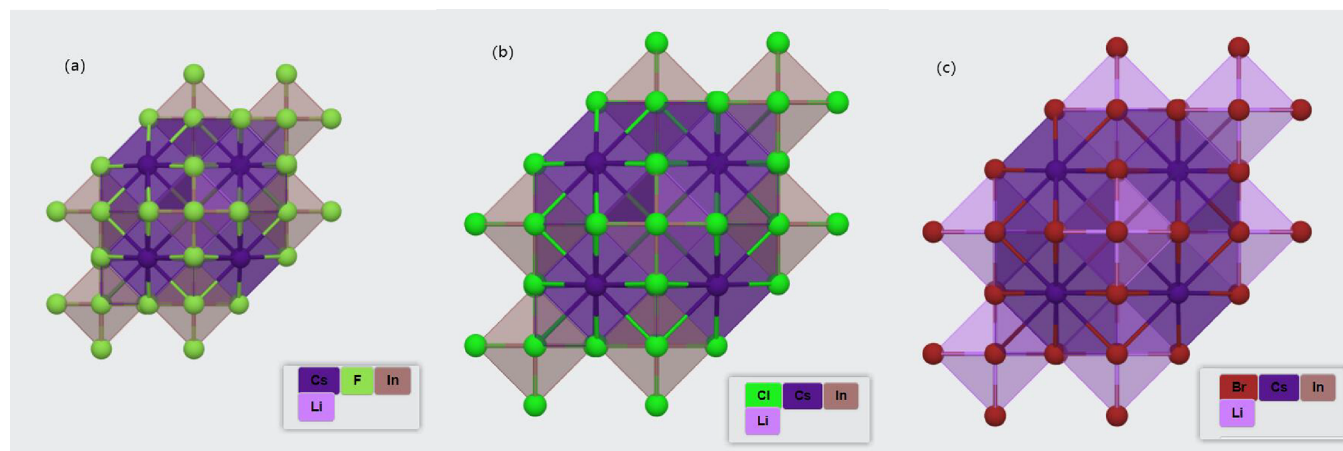
Figure 1. Schematic crystal structure of Cs$_2$LiInF$_6$ (a), Cs$_2$LiInCl$_6$ (b), and Cs$_2$LiInBr$_6$ (c). For clarity, the ball-and-stick model is displayed.

cadmium, thallium, or mercury. Among a large number of compounds examined, lead-free halogenated double perovskite, indium-, and silver-based perovskites have been more studied due to their excellent properties. For example, Shalan[17] et al. introduced a passivation molecule based on linear dicarboxylic acid, glutaric acid, through a simple anti-solvent additive engineering strategy to simultaneously improve the efficiency (22%) and long-term stability of the subsequent PSC. It not only enhances the humidity stability but also achieves considerable operational stability after aging for 2400 h under continuous lighting. Wang[18] et al. fabricated Cs$_2$AgBiCl$_6$ perovskite films by vapor deposition and demonstrated self-powered Cs$_2$AgBiCl$_6$ ultraviolet (UV) photodetectors with a high selectivity centered at 370 nm, low dark current density ($\approx$10^{-7} mA cm^{-2}), high optical emissivity ($\approx$10 mA W^{-1}), and detection rate ($\sim$1012 Jones) using a diode structure. The discovery of double perovskite lead-free halide provides a feasible way to find an air-stable and environment-friendly UV detector. Its novel physical properties make it an important position in the application of photovoltaic (PV) and thermoelectric materials. The understanding of the properties of double perovskite is still in its infancy, and there are still many problems to be discussed. The optical detection in the "solar blind" band (usually to a wavelength of <290 nm) has a wide range of applications, including deep ultraviolet radiation monitoring, flame sensing, rocket and missile early warning, non-line of sight optical communication, and environmental monitoring, which makes the development of broadband ultraviolet detector materials particularly important.

High-resolution, sharp luminescence spectra were observed for Cs$_2$LiInCl$_6$ at low temperatures, making it a promising competitor for lead-based halide chalcogenides used in photodetectors.[19−21] This work is devoted to exploring the properties of the wideband double perovskite candidate material Cs$_2$LiInX$_6$(X = F, Cl, and Br) and its possibility as a UV detector material. The architecture of assembling the UV detector based on Cs$_2$LiInX$_6$ aims to achieve a high sensitivity and detection rate. The electronic structure and energy band offset are evaluated by first-principles calculation to provide reliable information for improving the theoretical guidance of experiments. We have carried out in-depth theoretical research on Cs$_2$LiInX$_6$(X = F, Cl, and Br) and comprehensively studied the optical properties and stability of Cs$_2$LiInX$_6$(X = F, Cl, and Br) through first-principle calculation. The geometric structure

of Cs$_2$LiInX$_6$(X = F, Cl, and Br) plays an important role in its stability and luminescence properties. Therefore, it provides ideas and insights for the experiment and design of Cs$_2$LiInX$_6$(X = F, Cl, and Br) to obtain better performance in the potential applications of the ultraviolet, photon, and ionizing radiation detectors.

2. COMPUTATIONAL DETAILS

The calculation in this paper is carried out by the CASTEP module in the first-principles (DFT) package Materials Studio. Because the Kohn−Sham scheme based on the LDA and GGA functional will greatly underestimate the bandgap, a DFT error of up to 50% in the calculated bandgap energy is unacceptable. To understand the characteristics of semiconductors and insulators, it is often necessary to accurately describe the details of electronic structures.[22,23] We use the HSE06 scheme in the non-local exchange−correlation functional to deal with the bandgap problem. The interactions between electrons and ionic solids were described by the norm-conserving pseudo-potentials. All of the following results set the truncation energy of the plane-wave basis set to 400 eV and sample 3 × 3 × 3 from point K in the Brillouin zone. The test results show that this set of parameters can make the total energy of the system converge. The convergence of ionic structural relaxation is based on the fact that the force exerted on each atom is less than 1.0×10^{-2} e V/Å.

3. RESULTS AND DISCUSSION

3.1. Crystal Structure of Samples. In the elpasolite system, the halide ions surround the rare-earth ions, also known as the primary structure, especially A$_2$BReX$_6$, many of which have an aspect centric structure, and Re^{3+} ions have O-h symmetry and are far apart from each other. These structures can be interpreted as dense structures that belong to the perovskite family (cube and hexagon). The two "opposite positions" observed here are as follows: (1) all octahedrons have common angles leading to the constructed halide, and (2) all octahedrons have a common face, belonging to chain-containing halide groups. The number of octahedral holes surrounded by six X$^-$ anions is equal to the number of layers. Therefore, the A$_2$BReX$_6$ compound contains four molecular formula units in the axial heart unit, with eight octahedral spaces, of which four are occupied by B$^+$, the other four are occupied by Re^{3+}, and B$^+$ and Re^{3+} are surrounded by the X$^-$
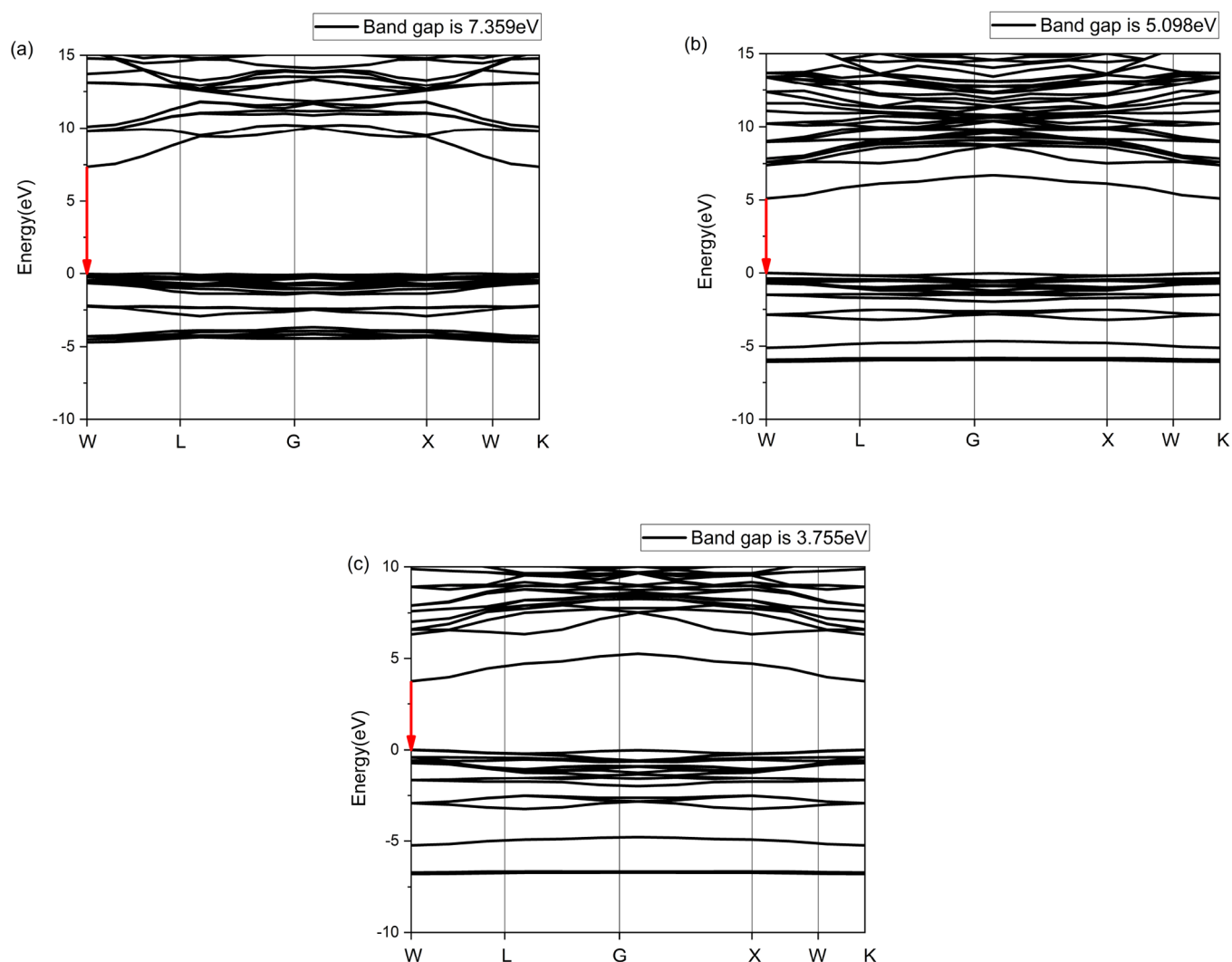
Figure 2. Band structure of Cs_2LiInF_6 (a), $Cs_2LiInCl_6$ (b), and $Cs_2LiInBr_6$ (c).

octahedron. The stability of the cubic elpasolite type is limited when B^+ and Re^{3+} become too small or A^+ and/or X^- become too large and polarized. Two variants of $Cs_2LiInCl_2$ have been observed in $Fm3m$ (225) and $R3m$ (166). Cs_2LiInX_6(X = F, Cl, and Br) with a structure type K is stacked in ...ABCABC... = c6, and the space group is $Fm3m$ (225). Cs_2LiInX_6 (X = F, Cl, and Br) consists of a three-dimensional network composed of InX_6 and LiX_6 octahedrons. There are Cs^+ ions in the gap, a total of 143 atoms, and 258 bonds. With the increase in the halogen atomic number, the halogen atomic radius increases, leading to the increase in the lattice constant and cell volume, as shown in Figure 1.

3.2. Band Structure and Density of States of Samples. The width of the energy band plays an important role in the properties of materials. For example, the width of the bandgap determines the utilization of light energy. The wider the band is, the greater the fluctuation in the band diagram is, indicating that the electrons in this band have a smaller effective mass, a greater degree of non-localization of electrons, and stronger expansibility of the atomic orbitals that make up this band. Figure 2 shows the band structure diagram of Cs_2LiInX_6 (X = F, Cl, and Br) and the symmetry points in the Brillouin region. The lower edge of the conduction band (VBM) is situated in the W point, and the upper edge of the valence band (CBM) is

also located at the W point. Both Cs_2LiInX_6 (X = F, Cl, and Br) show direct transition bandgap properties, which improves the photovoltaic quantum effect. Thus, the efficiency of photovoltaic conversion is improved, and the photoluminescence effect caused by carrier transmission along the indirect bandgap is avoided, which consumes the energy of the carrier and causes carrier annihilation. Therefore, direct bandgap materials are suitable for photovoltaic applications. Cs_2LiInF_6 has a bandgap of 7.359 eV, $Cs_2LiInCl_6$ has a bandgap of 5.098 eV, and $Cs_2LiInBr_6$ has a bandgap of 3.755 eV. Due to the low bandwidth of some current UV detectors, only some of them can be used for UV detection. In addition, the low bandgap reduces UV photosensitivity and avoids wavelength cutoff in the UV region. Therefore, Cs_2LiInX_6 (X = F, Cl, and Br) as a UV detector has an appropriate bandgap value and can realize high-performance UV detection. In Cs_2LiInX_6 (X = F, Cl, and Br), the bandgap value of Cs_2LiInX_6 (X = F, Cl, and Br) is effectively reduced by completely replacing Cl and F atoms with Br atoms with a large radius, which decreases the band minimum value (CBM) gradually, while the maximum value (CBM) of the valence band almost remains unchanged.

The energy levels in the valence band region are very narrow and very slow and smooth, while the conduction band region is wide and fluctuates greatly, which indicates that the effective
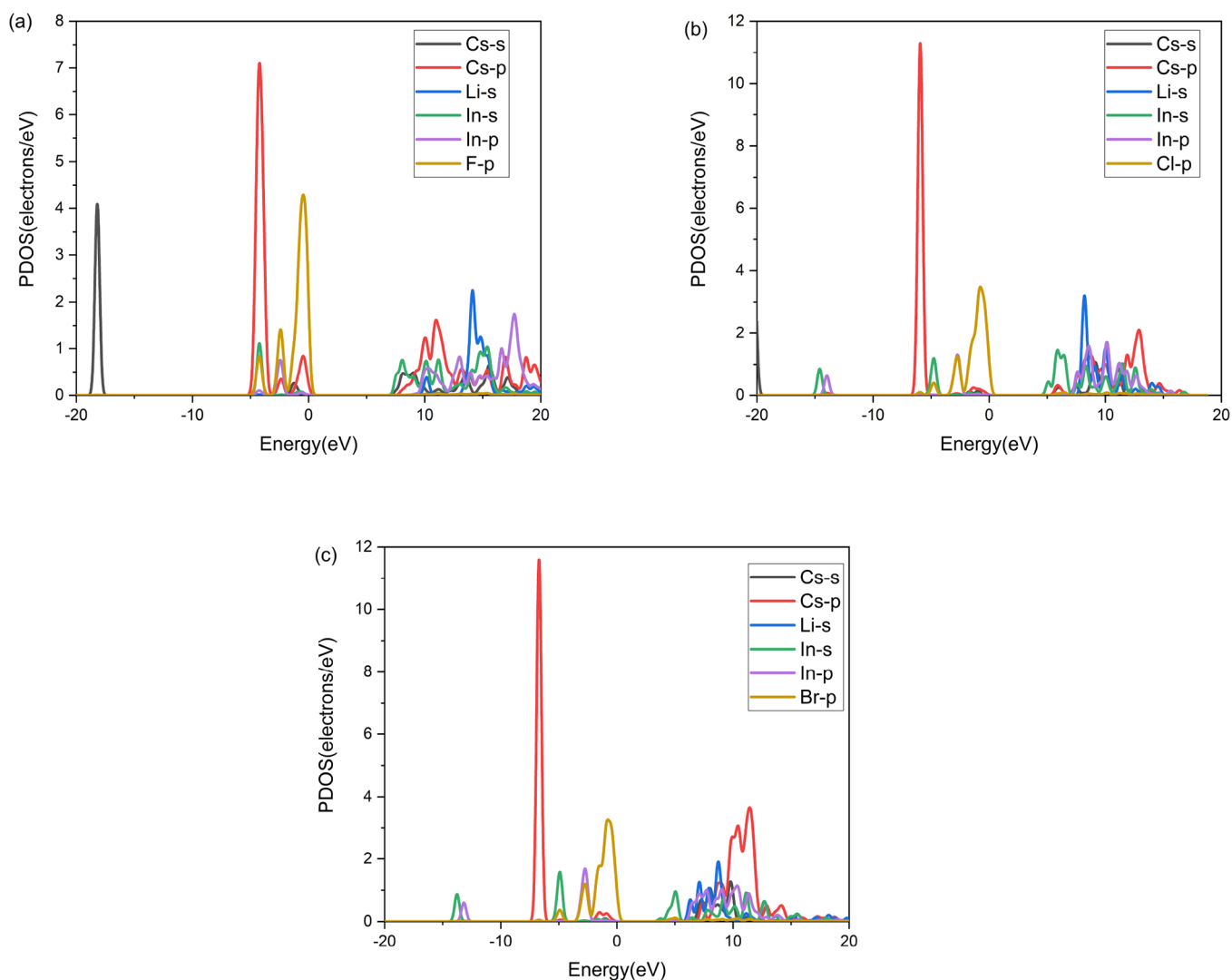
Figure 3. Partial density of states of Cs_2LiInF_6 (a), $Cs_2LiInCl_6$ (b), and $Cs_2LiInBr_6$(c).

mass of electrons in the conduction band is very small, the non-local density plays a big role, and the atomic orbital components that make up the conduction band are highly expandable. As can be seen from the density of states in Figure 3, near the Fermi level, the conduction band (7.22−9.64 eV) of Cs_2LiInF_6 is mainly composed of In-s, Cs-s, and Cs-p; the conduction band (4.61−7.13 eV) of $Cs_2LiInCl_6$ is mainly composed of In-s; and the conduction band (3.51−5.71 eV) of $Cs_2LiInBr_6$ is mainly composed of In-s. The valence band −1.81-0 eV of Cs_2LiInF_6 is mainly composed of F-p, and the electrons in F-p and In-p states are strongly hybridized within −3.17 to −1.81 eV. The valence band −2.10 to 0 eV of $Cs_2LiInCl_6$ is mainly composed of Cl-p, and the Cl-p and In-p electron states are strongly hybridized within −3.87 to −2.10 eV. The valence band −2.01 to 0 eV of $Cs_2LiInBr_6$ is mainly composed of Br-p, and there is a strong hybridization between Br-p and In-p electrons within −3.71 to −2.01 eV. The results show that the p-orbitals of halide ions and In ions are strongly hybridized in this region, which leads to the existence of several relatively flat bands in the corresponding energy range. The atomic wave function overlaps greatly in this region corresponding to the energy band structure diagram. The absorption of light is due primarily to the transition from the p-orbit of halide ions to the In-s orbit. In other words, the p-

orbitals of halide ions and the s-orbitals of In ions play a vital role in the light collection. It is well known that the more dispersed valence band and conduction band are more conducive to the mobility of photogenerated holes and electrons, respectively, to improve the luminous intensity and luminous efficiency.

3.3. Optical Properties. Another important characteristic of ultraviolet photodetector devices is the optical absorption coefficient. Figure 4 shows the calculated absorption spectrum of Cs_2LiInX_6 (X = F, Cl, and Br). It is observed that different halogen atoms have a great influence on the absorption coefficient. The addition of Br makes the absorption edge redshift so that Cs_2LiInX_6 (X = F, Cl, and Br) realizes visible light response. The light absorption coefficient of $Cs_2LiInBr_6$ in the visible regions is higher than that of $Cs_2LiInCl_6$ and Cs_2LiInF_6. In the ultraviolet part shorter than 193.15 nm (Cs_2LiInF_6) and 283.11 nm ($Cs_2LiInCl_6$), the ultraviolet detector made of $Cs_2LiInCl_6$ and Cs_2LiInF_6 has a great spectral response and is not sensitive to visible and infrared light, which is very important for detecting ultraviolet radiation in the background of visible and infrared light. The compound has great application potential in optoelectronic devices. Therefore, in the structure of Cs_2LiInX_6, changing halogen atoms can effectively improve the optical properties. $Cs_2LiInCl_6$ and
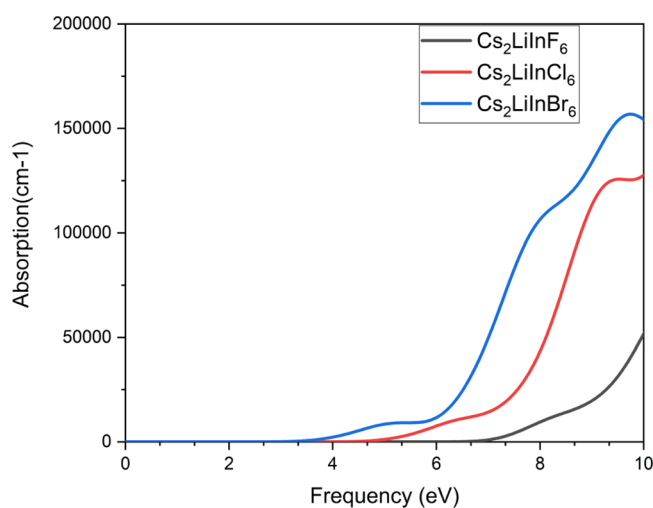
Figure 4. Absorption spectrum of Cs_2LiInX_6 (X = F, Cl, and Br)

Cs_2LiInF_6 are considered to be the most promising candidates for ultraviolet detectors.

3.4. Stability of the Samples. To explore whether Cs_2LiInX_6 (X = F, Cl, and Br) will produce phase change under high pressure, we optimized and calculated Cs_2LiInX_6 (X = F, Cl, and Br) under 0−100 GPa. Figure 5a−c analyzes the relationship between the unit cell lattice parameters and pressure in detail. The lattice parameters a, b, and c decrease upon bringing pressure to bear. The lattice constants a, b, and c of $Cs_2LiInBr_6$ are significantly distorted at 10 and 95 GPa, and the lattice constants a, b, and c of Cs_2LiInF_6 are distorted at 85 GPa. $Cs_2LiInCl_6$ shows a relatively stable state at 0−100 GPa.

Figure 6a−c analyzes the relationship between the lattice angle and the pressure in detail. It can be seen that the angle increases with the increase in pressure, but too much distortion has occurred for $Cs_2LiInBr_6$, and the changes of α, β, and γ are the same, but the range of distortion is within 0.062%, which is a small distortion; $Cs_2LiInCl_6$ maintains a stable state in a range of 0−75 GPa, and a large distortion appears at 90 GPa, the changes of α, β, and γ are the same, and the distortion range is within 0.025%; the α, γ, β of Cs_2LiInF_6 has obvious distortion at 25 and 60 GPa, and α, γ, and β have different changes at the distortion position, but the overall distortion range is within 0.017%.

Figure 7 analyzes the relationship between the unit cell volume and pressure in detail. The cell volume decreases with the increase in pressure. The crystal lattice volume of $Cs_2LiInBr_6$ has obvious distortion at 10 and 95 GPa, and the
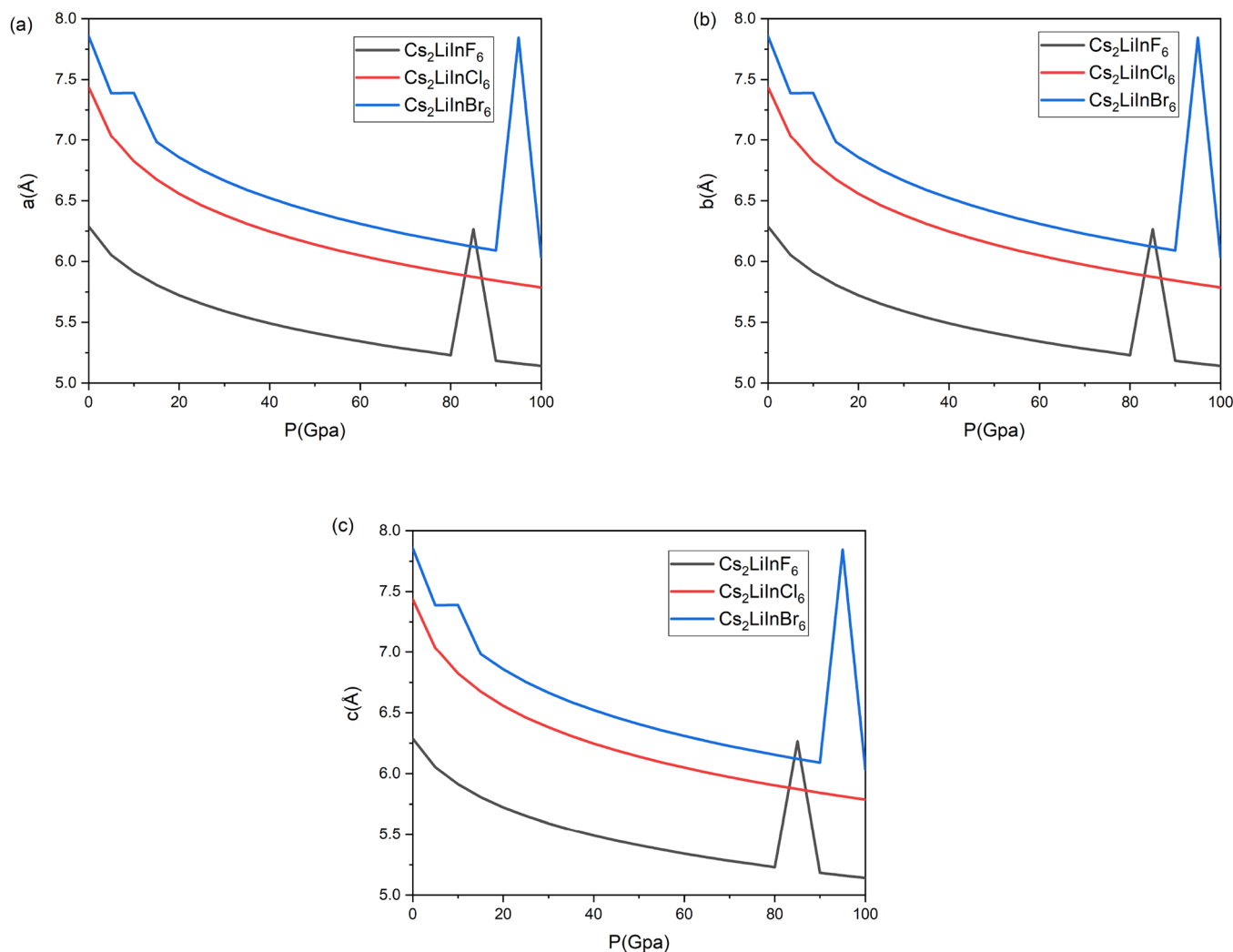

Figure 5. Variation of lattice constant under different pressures of Cs_2LiInF_6 (a), $Cs_2LiInCl_6$ (b), and $Cs_2LiInBr_6$ (c).
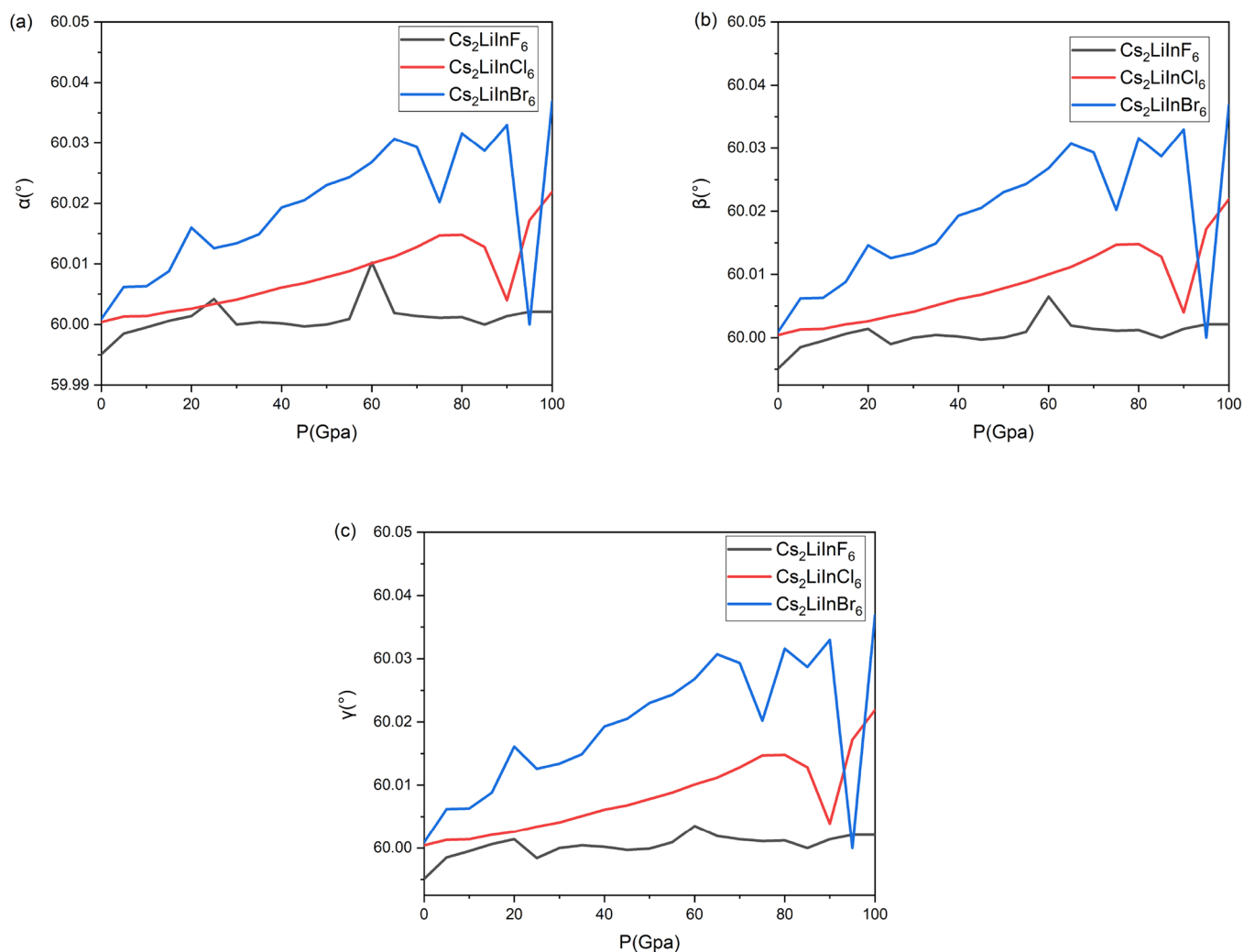
Figure 6. Variation of angle under different pressures of Cs_2LiInF_6 (a), $Cs_2LiInCl_6$ (b), and $Cs_2LiInBr_6$ (c).
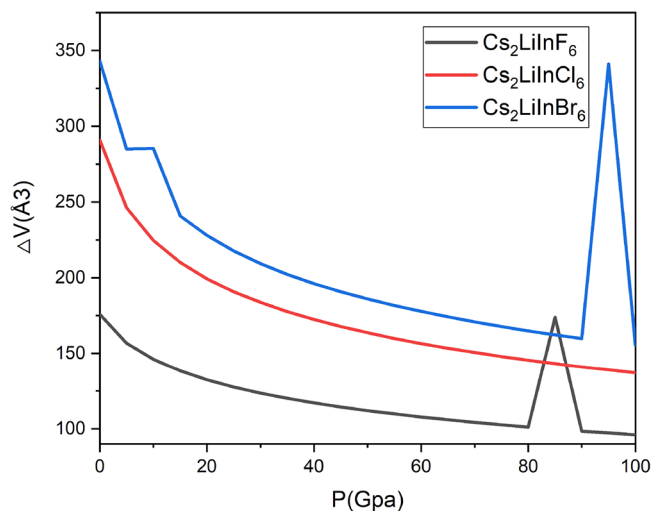

Figure 7. Variation of volume under different pressures of Cs_2LiInX_6 (X = F, Cl, and Br).

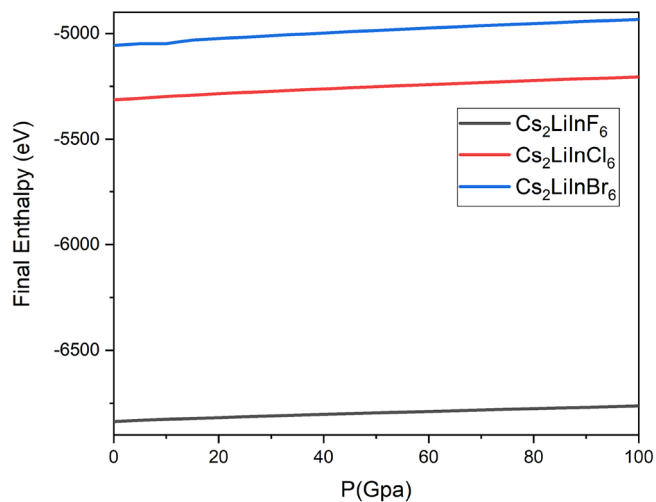**Figure 8.** Variation of volume under different pressures of Cs_2LiInX_6 (X = F, Cl, and Br).

crystal lattice volume of Cs_2LiInF_6 has obvious distortion at 85 GPa. $Cs_2LiInCl_6$ shows a relatively stable state at 0−100 GPa.

Figure 8 details the relationship between the final enthalpy and pressure. The volume of the unit cell decreases with the increase in pressure, but the slope is the same, and the stability under high pressure and low pressure is the same. This may be one of the reasons why this series of substances is difficult to synthesize. At the position where the lattice constant and the

angle of the unit cell are distorted, the energy increase does not cause distortion. However, it is worth noting that the final enthalpy of Cs_2LiInF_6 is the lowest and shows obvious relative stability. The final enthalpies of $Cs_2LiInBr_6$ and $Cs_2LiInCl_6$ are close, which proves that the stability of the cubic phase decreases with the increase in the X^- anion size.

In general, $Cs_2LiInCl_6$ has a low sensitivity to pressure and is relatively stable under a pressure of 0−100 GPa. Although the final enthalpy of Cs_2LiInF_6 is lower than that of $Cs_2LiInBr_6$ and $Cs_2LiInCl_6$, under certain pressure (at 25, 60, and 85 GPa), the lattice will be distorted.

3.5. Thermodynamic Properties. The Debye temperature is a significant indicator of the binding force of reactive molecules. The heat capacity of a substance provides information about vibration properties and energy band structures. To obtain Cs_2LiInX_6 (X = F, Cl, and Br), thermodynamic parameters (such as Debye temperature Θ and constant volume heat capacity (C_v)), we use the quasi-simple Debye model to study the thermodynamic properties of materials. The heat capacity C_v (formula 1) and Debye temperature (formula 2) can be expressed as

$$C_v = 3nk\left[4D\left(\frac{\Theta}{T} - \frac{\frac{3\Theta}{T}}{e^{\Theta/T} - 1}\right)\right] \tag{1}$$

where $D\left(\frac{\Theta}{T}\right)$ represents the Debye integral.

$$\Theta = \frac{\hbar}{k}[6\pi^2 V^{1/2} n]^{1/3} f(\sigma)\sqrt{\frac{B_S}{M}} \tag{2}$$

In the formula, M is the molecular mass per formula unit, B_S is the adiabatic bulk modulus, n is the number of atoms in the formula unit, and $f(\sigma)$ is given by formula 3, where σ is Poisson's ratio and takes 0.25

$$f(\sigma) = \left\{3\left[2\left(\frac{2}{3}\frac{1+\sigma}{1-\sigma}\right)^{3/2} + \left(\frac{1}{3}\frac{1+\sigma}{1-\sigma}\right)^{3/2}\right]^{-1}\right\}^{1/3} \tag{3}$$

For the specific heat capacity, when the temperature is higher than the Debye temperature, the specific heat capacity of the solid conforms to the Dulong−Petit law. CV does not depend on the temperature and converges to a constant 3R, that is, $C_v = 3R$ (C_v is the specific constant volume heat capacity, and R is the general gas constant); the specific heat capacity tends to be stable, which is due to the influence of anharmonic effect, which leads to the specific heat capacity almost close to the Dulong−Petit value, this part is mainly determined by the thermal vibration of the lattice; when the temperature is lower than the Debye temperature, the specific heat capacity follows the quantum law. The specific heat capacity is proportional to the cubic of the temperature $[C(T) \propto T^3]$. This is explained by the fact that when the temperature is low, the heat capacity of a solid is combined with the thermal vibration of the crystal lattice and the thermal motion of electrons, and the heat capacity increases faster.

Figure 9 shows the relationship between the heat capacity and temperature (0−1000 K). The results show that the heat capacity of the three structures has a similar trend, that is, as the temperature increases, the heat capacity C_v increases. When the temperature of Cs_2LiInF_6 is between 0 and 563 K, the specific heat capacity increases as the temperature rises, and the slope of the curve changes from large to small,
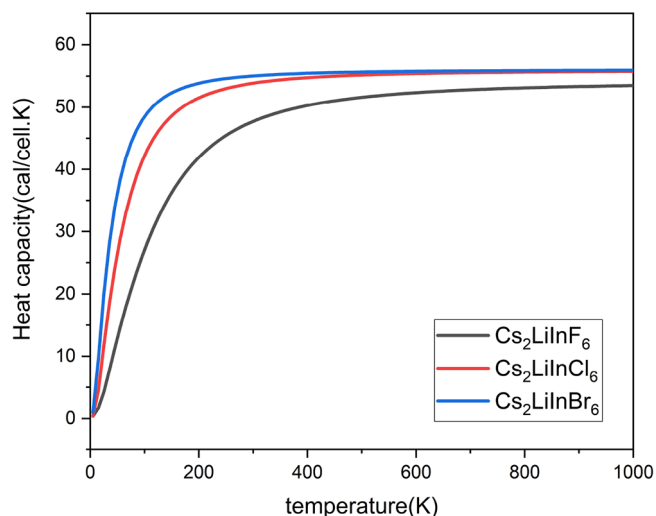

Figure 9. Temperature dependence of the heat capacity of Cs_2LiInX_6 (X = F, Cl, and Br).

gradually showing a trend of saturation and finally approaching a constant around 800 K. When the temperature of $Cs_2LiInCl_6$ is between 0 and 252 K, the specific heat capacity increases as the temperature rises, and the slope of the curve changes from large to small, gradually showing a trend of saturation and finally approaching a constant around 457 K. When the temperature of $Cs_2LiInBr_6$ is between 0 and 193 K, the specific heat capacity increases as the temperature rises, and the slope of the curve changes from large to small, gradually showing a saturation trend and finally approaching a constant around 266 K. Below 200 K, the C_v value of Cs_2LiInF_6 is the lowest, and the C_v value of $Cs_2LiInBr_6$ is the highest. As the temperature increases, the C_v value of $Cs_2LiInCl_6$ and $Cs_2LiInBr_6$ tends to be the same. At a sufficiently high temperature, C_v has little dependence on temperature and converges to a constant 3R, which conforms to the Dulong−Petit law.

The higher the melting point of a substance, the stronger its atomic bonding force and the higher the Debye temperature. The variation law of temperature and Debye temperature is illustrated in Figure 10. The calculated Cs_2LiInF_6 Debye temperature at 0 K is about 117.1859 K, the $Cs_2LiInCl_6$ Debye

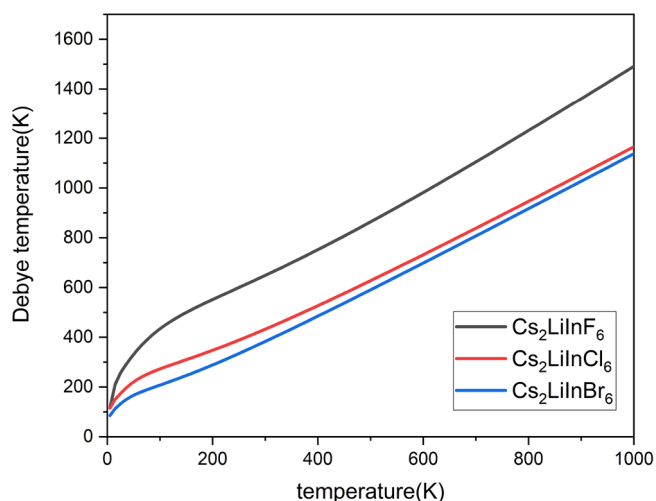**Figure 10.** Temperature dependence of the Debye temperature of Cs_2LiInX_6 (X = F, Cl, and Br).

temperature is about 115.23629 K, and the $Cs_2LiInBr_6$ Debye temperature is about 84.98422 K. Cs_2LiInF_6 has a higher Debye temperature, so its internal covalent bond is stronger than the other two structures. The Debye temperature increases with temperature under constant pressure, and the relationship between the Debye temperature and temperature is almost linear. In the search for new phosphors, studies have shown that materials with high fluorescence intensity and with high photoluminescence quantum yield Φ can be identified by searching for structurally rigid host compounds with high atomic connectivity. The Debye temperature (ΘD) of the material is the most reliable representative of the structural stiffness so that materials with a higher Φ value can be screened out. A higher ΘD tends to have higher energy phonon modes by suppressing the soft phonon mode without radiation relaxation, and the photoluminescence quantum yield Φ is enhanced, thereby increasing the tendency of photon emission, while low ΘD that often contains higher soft phonon mode can promote non-radiative relaxation. In the composition with the large bandgap and the high Debye temperature, Cs_2LiInF_6 has shown amazing potential.

4. CONCLUSIONS

Taking the lead-free halide perovskite semiconductor Cs_2LiInX_6 (X = F, Cl, and Br) as the research object, the molecular crystal structure model of the corresponding lead-free halide perovskite semiconductor material is established, and the first-principles density functional theory is adopted. Theory, calculated energy band, the density of state, optical properties, and thermodynamic properties further studied the influence of Cs_2LiInX_6 (X = F, Cl, and Br) under different pressures. The study revealed that the bandgap of Cs_2LiInF_6 is 7.359 eV, the bandgap of $Cs_2LiInCl_6$ is 5.098 eV, and the bandgap of $Cs_2LiInBr_6$ is 3.755 eV. The Br atom with a large radius completely replaces the Cl and F atoms, thereby effectively reducing the Cs_2LiInX_6 (X = F, Cl, and Br) bandgap value, and the bandgap value is small (3.755 eV); Cs_2LiInX_6 (X = F, Cl, and Br) with a direct bandgap is just the best candidate for making an ultraviolet detector. The absorption of light is due primarily to the transition from the p-orbital of the halide ion to the In-s orbital. The p-orbital of the halide ion and the s-orbital of the In ion play a vital role in the light collection. In the structure of Cs_2LiInX_6, changing halogen atoms can effectively improve the optical properties. $Cs_2LiInCl_6$ and Cs_2LiInF_6 are considered to be the most promising candidates for ultraviolet detectors. Among them, $Cs_2LiInCl_6$ has low relative pressure sensitivity and remains relatively stable under a pressure of 0−100Gpa. It is also found that Cs_2LiInF_6 shows amazing potential in phosphors with high photoluminescence quantum yield in components with a large bandgap and high Debye temperature. Our research has a good reference value for the preparation of lead-free perovskite-based ultraviolet detector devices with excellent subsequent preparation properties.

■ AUTHOR INFORMATION

Corresponding Author

    Jiaolian Luo − *School of Materials Science and Engineering, Guizhou Minzu University, Guiyang 550025, China; Special and Key Laboratory of Guizhou Provincial Higher Education for Green Energy-Saving Materials, Guiyang 550025, China;* ◉ orcid.org/0000-0001-5216-5761; Email: ljl612856@ 163.com

Authors

    Anqi Yang − *Special and Key Laboratory of Guizhou Provincial Higher Education for Green Energy-Saving Materials, Guiyang 550025, China; College of Big Data and Information Engineering, Guizhou University, Guiyang 550025, China*

    Zhenyu Xie − *Special and Key Laboratory of Guizhou Provincial Higher Education for Green Energy-Saving Materials, Guiyang 550025, China*

Complete contact information is available at:
https://pubs.acs.org/10.1021/acsomega.1c03342

Notes

The authors declare no competing financial interest.

■ ACKNOWLEDGMENTS

■ REFERENCES

(1) Guo, F.; Yang, B.; Yuan, Y.; Xiao, Z.; Dong, Q.; Bi, Y.; Huang, J. A nanocomposite ultraviolet photodetector based on interfacial trapcontrolled charge injection. *Nat. Nanotechnol.* 2012, 7, 798−802.

(2) Liu, X.; Gu, L.; Zhang, Q.; Wu, J.; Long, Y.; Fan, Z. All-printable band-edge modulated ZnO nanowire photodetectors with ultra-high detectivity. *Nat. Commun.* 2014, 5, 4007.

(3) García de Arquer, P.; Armin, A.; Meredith, P.; Sargent, E. H. Solution processed semiconductors for next-generation photo-detectors. *Nat. Rev. Mater.* 2017, 2, 16100.

(4) Yang, W.; Hu, K.; Teng, F.; Weng, J.; Zhang, Y.; Fang, X. High-performance silicon-compatible large-area UV-to-visible broadband photodetector based on integrated lattice-matched type II Se/n-Si heterojunctions. *Nano Lett.* 2018, 18, 4697−4703.

(5) Zhang, Y.; Li, S.; Li, Z.; Liu, H.; Liu, X.; Chen, J.; Fang, X. High-Performance Two-Dimensional Perovskite $Ca_2Nb_3O_{10}$ UV Photo-detectors. *Nano Lett.* 2020, 12, 382.

(6) Cai, S.; Xu, X.; Yang, W.; Chen, J.; Fang, X. Materials and designs for wearable photodetectors. *Adv. Mater.* 2019, 31, 1808138.

(7) Lin, Z.; Liu, Y.; Halim, U.; Ding, M.; Liu, Y.; Wang, Y.; Jia, C.; Chen, P.; Duan, X.; Wang, C.; et al. Solution-processable 2D semiconductors for high-performance large-area electronics. *Nature* 2018, 562, 254−258.

(8) Bae, S.-H.; Kum, H.; Kong, W.; Kim, Y.; Choi, C.; Lee, B.; Lin, P.; Park, Y.; Kim, J. Integration of bulk materials with two-dimensional materials for physical coupling and applications. *Nat. Mater.* 2019, 18, 550−560.

(9) Zhou, X.; Hu, X.; Zhou, S.; Song, H.; Zhang, Q.; Pi, L.; Li, L.; Li, H.; Lü, J.; Zhai, T. Tunneling diode based on WSe_2/SnS_2 heterostructure incorporating high detectivity and responsivity. *Adv. Mater.* 2018, 30, 1703286.

(10) Velusamy, D. B.; Haque, M. A.; Parida, M. R.; Zhang, F.; Wu, T.; Mohammed, O. F.; Alshareef, H. N. 2D Organic-Inorganic Hybrid Thin Films for Flexible UV-Visible Photodetectors. *Adv. Funct. Mater.* 2017, 27, 1605554.

(11) Xing, G.; Mathews, N.; Sun, S.; Lim, S. S.; Lam, Y. M.; Grätzel, M.; Mhaisalkar, S.; Sum, T. C. Long-Range Balanced Electron- and

Hole-Transport Lengths in Organic-Inorganic CH$_3$NH$_3$PbI$_3$. *Science* **2013**, *342*, 344−347.

(12) Akman, E.; Shalan, A. E.; Sadegh, F.; Akin, S. Moisture-Resistant FAPbI$_3$ Perovskite Solar Cell with 22.25% Power Conversion Efficiency through Pentafluorobenzyl Phosphonic Acid Passivation. *ChemSusChem* **2021**, *14*, 1176.

(13) Ozturk, T.; Akman, E.; Shalan, A. E.; Akin, S. Composition Engineering of Operationally Stable CsPbI$_2$Br Perovskite Solar Cells with a Record Efficiency over 17%. *Nano Energy* **2021**, *87*, 106157.

(14) Buin, A.; Pietsch, P.; Xu, J.; Voznyy, O.; Ip, A. H.; Comin, R.; Sargent, E. H. Materials Processing Routes to Trap-Free Halide Perovskites[J]. *Nano Lett.* **2014**, *14*, 6281−6286.

(15) Carrasco, L. R. Silver Lining of Singapore's Haze. *Science* **2013**, *341*, 342−343.

(16) Buin, A.; Pietsch, P.; Xu, J.; Voznyy, O.; Ip, A. H.; Comin, R.; Sargent, E. H. Materials Processing Routes to Trap-Free Halide Perovskites. *Nano Lett.* **2014**, *14*, 6281−6286.

(17) Shalan, A. E.; Akman, E.; Sadegh, F.; Akin, S. Efficient and Stable Perovskite Solar Cells Enabled by Dicarboxylic Acid-Supported Perovskite Crystallization. *J. Phys. Chem. Lett.* **2021**, *12*, 997−1004.

(18) Wang, M.; Zeng, P.; Wang, Z.; Liu, M. Vapor-Deposited Cs$_2$AgBiCl$_6$ Double Perovskite Films toward Highly Selective and Stable Ultraviolet Photodetector. *Adv. Sci.* **2020**, *7*, 1903662.

(19) Reber, C.; Güdel, H. U. Nonradiative relaxaetion processes in V^{3+} doped halide and oxide lattices[J]. *J. Lumin.* **1990**, *47*, 7−18.

(20) Reber, C.; Guedel, H. U.; Meyer, G.; Schleid, T.; Daul, C. A. Optical spectroscopic and structural properties of vanadium(3+)-doped fluoride, chloride, and bromide elpasolite lattices. *Inorg. Chem.* **1989**, *28*, 3249−3258.

(21) Meyer, G , Gaebell, H C . *Kubische und hexagonale Elpasolithe vom Typ Cs2LiMCl6 (M = Sc, Y, La-Nd, Sm-Lu, V, Cr, In)*; 1978.

(22) Gill, D.; Bhumla, P.; Kumar, M.; Bhattacharya, S. High-throughput screening to modulate electronic and optical properties of alloyed Cs$_2$AgBiCl$_6$ for enhanced solar cell efficiency. *J. Phys.: Mater.* **2021**, *4*, No. 025005. (10pp)

(23) Kumar, M.; Jain, M.; Singh, A.; Bhattacharya, S. Sublattice mixing in Cs$_2$AgInCl$_6$ for enhanced optical properties from first-principles[J]. *Appl. Phys. Lett.* **2021**, *118*, No. 021901.